NeuralSSD: A Neural Solver for Signed Distance Surface Reconstruction

Zi-Chen Xi, Jiahui Huang, Hao-Xiang Chen, Francis Williams, Qun-Ce Xu, Tai-Jiang Mu, Shi-Min Hu

Abstract—We proposed a generalized method, NeuralSSD, for reconstructing a 3D implicit surface from the widely-available point cloud data. NeuralSSD is a solver-based on the neural Galerkin method, aimed at reconstructing higher-quality and accurate surfaces from input point clouds. Implicit method is preferred due to its ability to accurately represent shapes and its robustness in handling topological changes. However, existing parameterizations of implicit fields lack explicit mechanisms to ensure a tight fit between the surface and input data. To address this, we propose a novel energy equation that balances the reliability of point cloud information. Additionally, we introduce a new convolutional network that learns threedimensional information to achieve superior optimization results. This approach ensures that the reconstructed surface closely adheres to the raw input points and infers valuable inductive biases from point clouds, resulting in a highly accurate and stable surface reconstruction. NeuralSSD is evaluated on a variety of challenging datasets, including the ShapeNet and Matterport datasets, and achieves state-of-the-art results in terms of both surface reconstruction accuracy and generalizability.

Index Terms—3D reconstruction, implicit surface, neural network, signed distance function, point cloud, sparse convolutional neural network

I. INTRODUCTION

SURFACE reconstruction from point clouds is a fundamental problem in 3D vision and graphics. In practice, point samples are often sparse, noisy, and incomplete due to sensor limitations, occlusions, and acquisition constraints, which makes faithful geometry recovery challenging. Recovering accurate surfaces from such data is critical in robotics, medical imaging, and interactive graphics, where geometric fidelity directly impacts downstream tasks and user experience. This paper targets robust reconstruction under these adverse conditions, aiming to recover watertight, detail-preserving surfaces from real-world point clouds.

Implicit representations—most commonly signed distance fields (SDFs) and occupancy—are widely adopted for surface reconstruction because they compactly encode complex geometry and naturally accommodate topology changes. In this work we adopt an SDF formulation for robustness and geometric expressiveness, while deferring a concise background on implicit fields and extraction algorithms to Section II.

Existing approaches fall into two families: optimization-based surface fitting and data-driven learning. Classical SDF/variational methods [1], [2] reconstruct by interpolating points with hand-crafted regularization to trade off smoothness and detail. These fixed priors are hard to tune, not data-adaptive, and under noisy or incomplete sampling often yield artifacts and limited generalization. Learning-based methods

either exploit the implicit bias of untrained networks [3]—requiring heavy per-scene optimization—or train feed-forward models from large datasets [4], [5]. Although efficient at inference, they lack mechanisms to guarantee tight adherence to input points and can inherit dataset biases [6], leading to over-smoothing or hallucinated structure.

To bridge these limitations, we propose NeuralSSD: a unified hybrid framework that couples an adaptive sparse convolutional predictor with a closed-form SDF fitting solver. The learned component produces a structure-aware sparse voxel scaffold (normals and basis functions), while the optimization component solves a variational fitting problem that explicitly balances data fidelity and learned priors. The solver is fully differentiable, enabling end-to-end training and yielding watertight, noise-robust reconstructions at scale; an overview is shown in Figure 1.

Briefly, NeuralSSD parameterizes the SDF as a spatially varying basis expansion predicted by an adaptive sparse convolutional network over a multi-scale voxel scaffold. Given raw points and inferred normals, a closed-form variational solver computes the basis coefficients with an interpretable regularization that balances data fidelity and learned priors. The pipeline is fully differentiable, enabling end-to-end training and scalable, watertight, detail-preserving reconstruction.

In summary, the contributions of NeuralSSD can be outlined as follows:

- Unified hybrid framework that enforces point-wise input fidelity while leveraging learned priors, resolving the fidelity-generalization trade-off under sparse/noisy sampling.
- A novel energy formulation that combines normal alignment, Hessian regularization, and point constraints, enabling robust reconstruction from noisy and sparse data.
- Adaptive sparse neural network that infer normals and spatially varying bases on a multi-scale voxel scaffold, scaling to large scenes and producing watertight, detailrich reconstructions.

Empirically, NeuralSSD delivers higher accuracy and watertightness under noise and incompleteness, while reducing perscene optimization time compared to purely optimizationbased methods; see Section IV.

II. RELATED WORKS

This section provides a review of both classical and recent surface reconstruction methods, with a specific focus on pointcloud-based approaches.

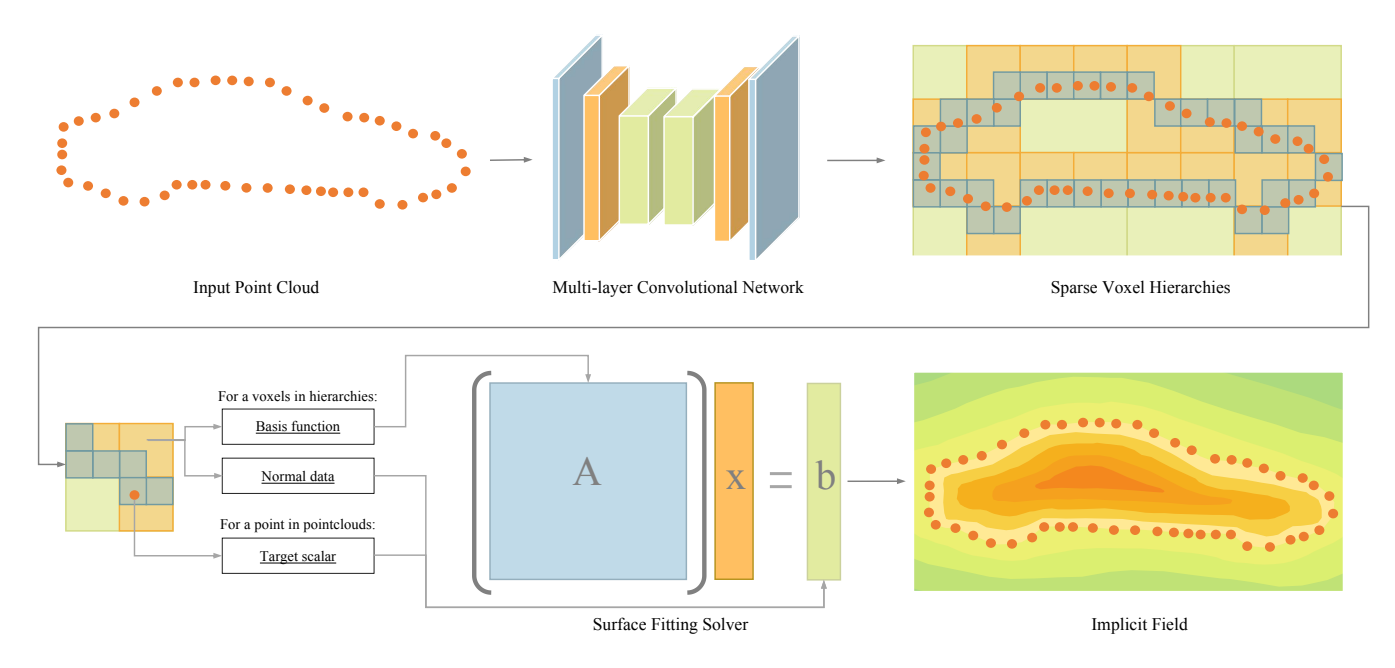


Fig. 1. The NeuralSSD pipeline. Given a raw point cloud, we first construct a multi-scale sparse voxel grid. An adaptive sparse network then predicts spatially varying basis functions and normals within this grid. Finally, a closed-form, differentiable SDF solver computes the basis coefficients to reconstruct a watertight surface. This hybrid approach combines a learned, structure-aware prior with a variational optimization that explicitly enforces data fidelity, enabling robust and detailed reconstruction from sparse and noisy inputs.

A. Background: Implicit Surface Representations

An implicit surface defines a shape as the level set of a scalar field f, commonly at threshold $\delta = 0$. Formally,

$$\mathcal{S} := \{ P \in \mathbb{R}^3 \mid f(P) = \delta \}. \tag{1}$$

where $P \in \mathbb{R}^3$ denotes a 3D point, $f : \mathbb{R}^3 \to \mathbb{R}$ is the scalar field (e.g., SDF), and $\delta \in \mathbb{R}$ is the level-set threshold (commonly 0). Two prevalent choices of f are signed distance fields (SDFs), which map each point to its signed distance to the surface (negative inside, positive outside), and occupancy fields, which indicate inside/outside with binary values. When a discrete approximation is required, the implicit surface can be extracted from a volumetric grid using algorithms such as Marching Cubes [7]. [8] is one of the earliest and foundational techniques, utilizes an analytic volumetric running mean fusion strategy to transform scan data into 3D models. To augment the method's robustness against noise and corrupted data, [2] incorporates radial basis function interpolates and addresses the reconstruction challenge through low-rank smoothness regularization. [9] adopt an approach of representing the shape via a combination of multiple parametric surfaces, which are fitted using local geometrical features. Our methodology is influenced by the study by [1], the SSD is employed to approximate the signed distance field through the resolution of a variational problem that leverages linear parameterization of function families. Poisson reconstruction [10] and its screened variant [11]involve solving partial differential equations (PDEs) to reconstruct surfaces from Hermite data. These techniques have proven to be empirically robust and effective under diverse conditions and have found widespread application in contemporary systems, as exemplified in [12].

B. Learning-Based Surface Reconstruction

Within the domain of learning-based 3D reconstruction, a myriad of strategies have been developed to optimally leverage data priors for enhanced reconstruction quality, facilitated by the advancement of deep learning technologies and the proliferation of extensive 3D datasets. [13] innovatively embedded the inductive bias directly within a 3D CNN architecture, eliminating the need for training data. The NKF framework [14] introduced a novel data-dependent kernel, offering improvements over traditional non-learned kernel methods that originate from infinitely wide ReLU networks, as discussed in Neural Splines [15], while NKSR [16] also utilizes a data-dependent kernel but limits its spatial extent to boost computational efficiency and employs a gradient-based fitting approach to enhance noise immunity. The concept of transforming 3D points into a feature grid through convolutional architectures was previously suggested in ConvONet [17] and CIRCLE [18] for predicting occupancy fields. POCO [19] enhanced the efficacy and performance of ConvONet by integrating a transformer architecture in place of conventional convolutions. However, both of these methods suffer from prolonged reconstruction times for even modest-sized scenes. In contrast, our feature mapping leverages a hierarchical sparse data structure for heightened efficiency. Sparse data structures have been explored in ASR [20] and DOGNN [21], which put forth octree-based convolutional architectures for the reconstruction of expansive scenes. Neural-IMLS [22] directly learns a noise-resistant signed distance function from unoriented raw point clouds in a self-supervised manner. DiGS [23] introduces a divergence-guided constraint to learn a high-fidelity representation from unoriented points, while OG-INR [24] employs an octree-guided approach to solve the ambiguity of inside/outside labeling for unoriented point

clouds. SSRNet [25] divided point clouds into different local parts and processes them in parallel. Shape as Points [26] employs a method to upsample input points followed by a differentiable Poisson reconstruction, a concept that NGSolver [27] expands upon by incorporating learnable basis functions. Point2mesh [28] demonstrated that mesh deformation over templates can yield high-quality reconstructions by naturally constraining the (self-)priors within the manifold of surfaces. The latest implicit representations, which utilize a singular feed-forward network to parameterize geometry [5] and [29], introduce novel constraints [30] and [31] to regularize training. Other works focus on the learning objective and process. For instance, Neural-Pull [32] introduces a differentiable operation to pull query points towards the surface. To handle noisy inputs, some methods propose to learn from noisy data directly, such as learning a noise-to-noise mapping [33] without clean supervision. ALTO [34] improves reconstruction fidelity and speed by alternating between different latent topologies. InstantNGP [35] leverages a multiresolution hash encoding to accelerate the training and rendering of neural graphics primitives by several orders of magnitude.

C. Neural Representations for Surfaces

In the realm of shape parametrization, recent scholarly works have extensively examined the application of neural networks. Various 3D data representations have been employed to enhance representational efficacy. Initial approaches like 3dr2n2 [4] utilized dense voxel grids. To improve efficiency, subsequent developments introduced sparse and hierarchical data structures such as octrees, as seen in OctNet [36] and O-CNN [37], or other adaptive voxel grids [38] to capture local variations. Vox-Surf [39] divides the space into sparse voxels that store geometry and appearance information on its corner vertices. Similarly, patch-based approaches have been proposed to leverage local details. Points2Surf [40] learns a prior over local patches combined with global information to improve generalization. DeepLS [41] stores a grid of latent codes, each representing a local SDF, to enable efficient and detailed reconstruction. The intricate nature of neural functions necessitates the imposition of regularization strategies to ensure surface smoothness [42]. Conversely, biases towards certain feature frequencies [43] [44] or multi-scale representations [45] [46] have been introduced to enhance the geometric detail in specific areas. BACON [47] introduces a network architecture with an analytical Fourier spectrum, allowing for better control over the spectral characteristics of the represented signal. A distinct strand of research addresses implicit fields more systematically: [15] presented a methodology to align an infinitely-wide network with point data interpolation via the kernel method, which was subsequently refined into a learnable model in [14]. ImplicitFilter [48] applied an implicit filter to smooth the field while preserving details. Diverging from direct neural network utilization for shape depiction, our approach employs a spatially-variable set of basis functions and resolves the surface fitting issue through a closed-form solution. Empirical evidence suggests that while our methods representational capacity mirrors that of the aforementioned techniques, it facilitates an optimal fit more readily, eliminating the need for labor-intensive optimizations.

III. METHOD

Our method predicts a continuous watertight 3D surface from a point cloud without normal. The method is based on the Neural Galerkin method, which is a variational formulation of the PDE that involves a neural network to infer a set of spatially-varying basis functions that discretize the target implicit field. Given a set of points $\mathcal{P} := \{P \in \mathbb{R}^3\}$, the method constructs a signed distance field on multi-layer sparse voxel hierarchy by a sparse convolutional network, to obtain an expressive surface representation. A mesh can later be constructed from the implicit surface representation using techniques such as the dual marching cubes algorithm.

In the following sections, we will describe the details of our method, and summarize the key steps in Figure 1.

A. Screened Poisson equation with Hessian regularization

Inspired by SPSR and SSD, we propose a new energy formulation for the surface reconstruction problem. The energy formulation is defined as:

$$E(f) = E_N(f) + \lambda_1 E_H(f) + \lambda_2 E_P(f), \tag{2}$$

where $E_N(f)$, $E_H(f)$, and $E_P(f)$ are the normal alignment, Hessian regularization, and point constraint energy terms, respectively, and $\lambda_1, \lambda_2 \in \mathbb{R}_{>0}$ are weighting factors.

$$E_N(f) = \iiint_{\Omega} \left\| \nabla f - \vec{\mathbf{N}} \right\|_2^2 dV, \tag{3}$$

where ∇f is the gradient of the implicit field f, \vec{N} is the predicted unit normal field, and the integral is over the 3D domain Ω .

In Eq (2), the first term $E_N(f)$ is the integration of the L2-norm of the difference between the gradient ∇f and the normal field \vec{N} in the 3D domain of Ω , which measures the alignment between the surface and the level of the normal field. By promoting non-zero values exclusively at the shape boundary, we encourage \vec{N} to generate a reconstructed field that closely resembles a smoothed indicator function. When integrated across the entire domain, this term contributes to an overall estimation of the shape's orientation, with a strong regularization effect imposed by the normal field. This term is also known as the normal consistency term.

$$E_H(f) = \iiint_{\Omega} ||H(f)||_F^2 \, \mathrm{d}V, \tag{4}$$

where H(f) is the Hessian matrix of f and $\|\cdot\|_F$ denotes the Frobenius norm.

The second term, $E_H(f)$, is a Hessian energy term that regularizes the smoothness of the implicit field f. Minimizing the Frobenius norm of the Hessian matrix, $\|H(f)\|_F^2$, encourages the field's second derivatives to be close to zero. This property is characteristic of a true Signed Distance Function (SDF), which has a constant gradient magnitude of one, and therefore

a zero Hessian. This regularization is particularly crucial for our Galerkin framework; it ensures that the implicit function remains smooth and avoids spurious oscillations in regions far from the input points \mathcal{P} , a common challenge when using global basis functions. It acts as a powerful smoothness prior on the entire domain Ω , complementing the data-fitting terms without needing to estimate unstable geometric attributes like curvature directly from the sparse input points.

$$E_P(f) = \sum_{p \in \mathcal{P}} (f(p) - \xi(p))^2,$$
 (5)

The third term $E_P(f)$ of Eq (1) is the point constraints term, which measures the discrepancy between the implicit function f and the observed point cloud \mathcal{P} . The point constraints term is given by the L2-norm of the difference between the predicted values $\xi(p)$ and the observed values f(p). By minimizing this term, we can obtain a surface that is well-aligned with the input data. This term ensures that the surface closely matches the input points, acting as a strong constraint. Particularly in regions with intricate geometric details, these point constraints play a crucial role in achieving a tight fit, thereby enhancing the clarity and accuracy of surface details. The use of $\xi(p)$ primarily serves the purpose of denoising by allowing points to be located outside the surface. So the whole formulation could be expressed as:

$$E(f) = \iiint_{\Omega} \left\| \nabla f - \vec{\mathbf{N}} \right\|_{2}^{2} dV + \lambda_{1} \iiint_{\Omega} \left\| H(f) \right\|_{F}^{2} dV + \lambda_{2} \sum_{p \in \mathcal{P}} (f(p) - \xi(p))^{2}.$$
(6)

This formulation allows for a balanced integration of learned priors and data fitting. The regularization term in the equation ensures that the square norm of the Hessian matrix is close to zero, resulting in a nearly constant gradient for the function away from the data points. In the vicinity of the data points, the contribution from the data energy terms dominates the total energy, while the regularization energy term plays a bigger role away from the data points, leading to a constant gradient vector field ∇f . The Hessian regularization term encourages the surface to be smooth, while the signed distance error term encourages the surface to be as close as possible to the input point cloud. The entire formulation effectively achieves a balance between the model's data fitting capability and its generalization ability.

B. Discretized implicit field on sparse voxel hierarchies

Instead of converting point clouds into dense voxel grids or octree structures, we use a sparse voxel hierarchy required by our analytic solver. Local support of basis functions centered at voxel centroids yields a sparse, well-conditioned linear system $\mathbf{A}\alpha = \mathbf{b}$ solved directly; computation and memory scale with the number of active voxels via $\Omega = \bigcup Rgn(v)$; a sparse voxel backbone network selects and parameterizes active cells, predicting $\mathbf{m}_k^{\mathcal{S}}$ to inject learned priors while preserving the linear formulation. This design reduces cost

during both learning and solving and enables coarse-to-fine control where fine levels add details only where data exist.

Given a set of multi-layer sparse voxels $\mathcal{V}:=\{\mathcal{V}^1,\mathcal{V}^2,,...,\mathcal{V}^S\}$ where \mathcal{S} is the number of layers. Each voxel grid \mathcal{V}^S is a regular grid of voxels $\{v_k^S|k=1,2,...\}$ with a fixed size 2^{S-1} , where b is the base voxel size. The voxel grid \mathcal{V}^S is strictly contained within \mathcal{V}^{S+1} . Given a scaffold, we dynamically set the integration domain Ω as $\Omega:=\bigcup_{\mathcal{S}}\bigcup_{v_k^S\in\mathcal{V}^S}Rgn(v_k^S)$, where Rgn(v) represents the enlarged region spanned by the voxel v with a factor of 3^3 . To ensure an efficient solution to the problem described in equation (2) and maintain a high level of flexibility for surface representation, we define the target implicit function as follows:

$$f(\mathbf{p}) := \sum_{\mathcal{S}} \sum_{k} \alpha_{k}^{\mathcal{S}} \mathcal{B}_{k}^{\mathcal{S}}(\mathbf{p}),$$
with $\mathcal{B}_{k}^{\mathcal{S}}(\mathbf{p}) := B_{k}^{\mathcal{S}} \left(\frac{\mathbf{p} - Cntr(v_{k}^{\mathcal{S}})}{2^{\mathcal{S} - 1}} \right).$
(7)

The subscript k represents the sum over all voxels in $\mathcal{V}^{\mathcal{S}}$, and Cntr(v) denotes the centroid coordinate of voxel v. The function $B_k^{\mathcal{S}}:\mathbb{R}^3\to\mathbb{R}$ is the basis function that remains fixed during energy minimization. It exhibits spatial variation and, when multiplied by the coefficient $\alpha_k^{\mathcal{S}}\in\mathbb{R}$, describes the entire surface.

In contrast to the fixed Bézier tensor basis used in SPSR, we employ a parameterized family of basis functions that allows us to incorporate learned priors into the solution. The parameters of these basis functions are predicted by our upstream network, enabling the solver to flexibly incorporate inductive biases from the learned module.

$$B_k^s(\boldsymbol{p}) := B(\boldsymbol{p}; \boldsymbol{m}_k^s) := \begin{cases} \prod_{a \in \{x, y, z\}} b^{\mathbf{a}}(a; \boldsymbol{m}_k^s), & \boldsymbol{p} \in \Omega_B \\ 0, & \boldsymbol{p} \notin \Omega_B \end{cases},$$
$$b^{\mathbf{x}}(x; \boldsymbol{m}_k^s) := \sum_u m_u^x q_u^x(x), \quad m_u^x \in \mathbb{R}, \quad q_u^x : \mathbb{R} \mapsto \mathbb{R}, \quad (8)$$

where p = [x,y,z] denotes three-dimensional space with axes x,y, and z, and the domain $\Omega_x := [-1.5,1.5]$, which represents the support of the basis. We define functions $b^x(x)$, $b^y(y)$, and $b^z(z)$. And q_u are elementary functions that are blended by weights m_u s, which vary across voxels. The vectorized form $\boldsymbol{m}_k^{\mathcal{S}} := [\dots, m_u, \dots]^T$ parameterizes the continuous function $B_k^{\mathcal{S}}$. For more details about the basis function, please refer to the Appendix B.

Utilizing the Euler-Lagrange equation (the detailed derivations of which are provided in the Appendix A) and the aforementioned discretization scheme, we can determine the optimal surface fitting by solving the equation in closed-form. This involves finding the best possible linear coefficients

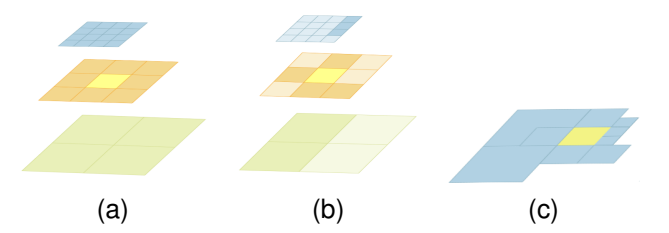


Fig. 2. When focusing on the two-dimensional special case for ease of understanding, the original multi-layer convolutional kernel consists of 29 elements, derived from layers of different sizes from three neighboring hierarchies, as illustrated in 2a. During the convolution operation, the voxels within the convolution kernel are filtered based on the number of points computed inside the voxel, as shown in 2b. This results in a convolutional kernel of the form 2c. The actual convolution process, however, occurs in three dimensions, where the original multi-layer convolutional kernel consists of 107 voxels, originating from three adjacent hierarchies.

 $\alpha := [..., \alpha_k^{\mathcal{S}}, ...]T$ for the implicit field f.

$$\mathbf{A}\boldsymbol{\alpha} = b,$$
with
$$\mathbf{A}_{(\bar{k},\bar{l})} = \iiint_{\Omega} \nabla \mathcal{B}_{\bar{k}}^{\top} \nabla \mathcal{B}_{\bar{l}} dV + \lambda_{2} \sum_{\bar{l}} \alpha_{\bar{l}} \iiint_{\Omega} \Delta \mathcal{B}_{\bar{k}} \cdot \Delta \mathcal{B}_{\bar{l}} dV + \lambda_{1} \sum_{\bar{l}} \alpha_{\bar{l}} \sum_{p \in \mathcal{P}} \mathcal{B}_{\bar{k}}(\boldsymbol{p}) \mathcal{B}_{\bar{l}}(\boldsymbol{p}),$$

$$b_{(\bar{k})} = \iiint_{\Omega} \nabla \mathcal{B}_{\bar{k}}^{\top} \vec{\mathbf{N}} dV + \lambda_{1} \sum_{p \in \mathcal{P}} \mathcal{B}_{\bar{k}}(\boldsymbol{p}) \xi(\boldsymbol{p}), \quad (9)$$

In this equation, the subscripts \overline{k} and \overline{l} represent the row and column indices of the matrix, respectively. The optimization problem takes into account all voxels across all scales, with \overline{k} and \overline{l} indexing the product of the subscripts k and s (i.e., \mathcal{B}_k^S is represented as $\mathcal{B}_{\overline{k}}$ as previously defined).

C. Multi-layer convolution

With an adaptive sparse neural network applied to sparse voxel hierarchies, the goal is to predict key attributes required by the surface fitting solver. This section primarily focuses on elucidating how the multi-layer convolution is employed to learn valuable priors from various layers.

To handle the adaptive grids with irregular spacing in the input point cloud, traditional regular 3D convolutions and even sparse convolutions are not suitable. Regular 3D convolutions can be expressed in the following formulation:

$$F_i = \sum_{j \in NB(i)} \mathbf{W}(\Delta p_{ij}) \times F_j, \tag{10}$$

Where F_i and F_j are the input and output features of the network, p_{ij} are the relative position of voxels v_i and v_j , W is the weight matrix of the network, NB(x) is the set of neighboring voxels of x. The regular 3D convolution expects data to be represented at regularly spaced points, while sparse convolutions assume regular grids and do not account for the irregular spacing found in adaptive grids. Both of them need to be addressed on the same layer of sparse voxels, which means that the input features are detailed when the input point clouds are dense around the output voxel, while input features

are rough when the input point clouds are sparse. In order to address the non-uniform distribution of point clouds and ensure a balanced aggregation of point information during each convolution, we introduce a multi-layer convolution approach at the voxel level. Figure 2(a) shows an example of the kernels. This allows for 3D convolutions to be performed on voxels across different layers, and can be expressed as:

$$F_i = F_i + \sum_{j \in NB(i)} \mathbf{W}(\Delta p_{ij}) \times \mathcal{C}(F_j^{down}, F_j^{cur}, F_j^{up}), \quad (11)$$

, where $\mathcal C$ is a convolutional kernel function that takes into account the spatial relationships between different layers.

$$\mathcal{C}(F_j^{down}, F_j^{cur}, F_j^{up}) := \begin{cases} F_j^{down}, & N_{v_j} > N_{max} \\ F_j^{cur}, & N_{min} < N_{v_j} < N_{max} \\ F_j^{up}, & N_{v_j} < N_{min} \end{cases}$$

Where N_{v_j} is the number of neighboring voxels of v_j in the down, current, and up directions, respectively. The convolutional kernel has 27 elements, one for each combination of neighboring voxels. During the convolution operation, it is possible to filter the voxels within the convolution kernel based on a pre-calculated number of points. Voxel features that meet the criteria will be retained, and ultimately, the features from 67 voxels in the upper and lower layers will be aggregated into a convolution kernel of size 27, provided that both upper and downer layers exist. We have incorporated residual connections to mitigate the issue of overfitting during the learning process of voxels across different layers.

D. Point-Voxel Attention

Voxel-based convolutional methods typically aggregate point features within each voxel into a single feature vector. This aggregation, while efficient, causes a loss of fine-grained geometric detail by discarding the spatial distribution of points within a voxel. Such information loss is detrimental for high-fidelity surface reconstruction. To address this, we introduce a Point-Voxel Attention mechanism as a complementary module to our sparse convolutional backbone. This mechanism refines voxel features by attending to the individual points they contain, thereby re-introducing crucial intra-voxel positional information.

Let $F_v \in \mathbb{R}^{C_v}$ be the feature of a voxel v, and let $\{p_j\}_{j=1}^{N_v}$ be the set of N_v points contained within this voxel, each with its feature $F_{p_j} \in \mathbb{R}^{C_p}$. Our goal is to update the voxel feature F_v by aggregating information from its constituent points in a spatially-aware manner.

The core idea is to compute attention weights for each point based on its features and relative position within the voxel. The updated voxel feature is then a weighted sum of point-derived values. The process is as follows:

First, we project the point and voxel features into a common embedding space to derive query (q), key (k), and value (u) vectors. The query and value vectors are derived from point features, while the key vector is derived from the voxel feature:

$$\mathbf{q}_i = \phi_q(F_{p_i}), \quad \mathbf{u}_i = \phi_u(F_{p_i}), \quad \mathbf{k}_v = \psi_k(F_v)$$
 (13)

where ϕ_q , ϕ_u , and ψ_k are implemented as simple multi-layer perceptrons (MLPs).

To incorporate crucial intra-voxel positional information, we compute a positional encoding F_{pos_j} from the relative coordinates $\delta_j = p_j - Cntr(v)$ of each point p_j with respect to the voxel center Cntr(v):

$$F_{\mathsf{pos}_{j}} = \phi_{\mathsf{pos}}(\boldsymbol{\delta}_{j}) \tag{14}$$

where ϕ_{pos} is another MLP.

The attention weight α_j for each point p_j is then computed based on the compatibility between the point's query and the voxel's key, modulated by the positional encoding:

$$w_j = \phi_w(\mathbf{k}_v - \mathbf{q}_j + F_{\mathsf{pos}_i}) \tag{15}$$

Here, ϕ_w is an MLP that maps the compatibility score to a single scalar. The weights are normalized across all points within the same voxel using the softmax function. Finally, the new voxel feature F_v' is computed by aggregating the point-based values, also enhanced with positional encoding, using the calculated attention weights:

$$F'_{v} = \sum_{j=1}^{N_{v}} \frac{\exp(w_{j})}{\sum_{i=1}^{N_{v}} \exp(w_{i})} (\boldsymbol{u}_{j} + F_{\text{pos}_{j}})$$
 (16)

This updated feature F_v' is then added to the original voxel feature F_v via a residual connection, enriching it with fine-grained, position-aware information from the raw point cloud. This mechanism allows the network to learn a more precise representation of the underlying surface geometry, complementing the broader contextual understanding provided by the sparse convolutions.

IV. EXPERIMENT

In this section, we introduce the experimental settings, including the parameters and evaluation metrics used in our experiments. We then present the results of our method at different scales, including object-level datasets and indoor scene datasets. We also conduct ablation studies and analyze the time and memory efficiency of our method.

A. Implementation Details

We implement our method based on a high-performance point cloud inference engine, Torchsparse [49] to accelerate the computation of neighborhood queries and sparse matrix operations, the sparse multi-layer convolutional network shares its neighborhood map with the linear solver. We use an AWSGrad optimizer [50] with a learning rate of 0.001 and a batch size of 1. In our experiments, we set the parameters as follows: $\lambda_1 = 64.0$, $\lambda_2 = 3.0$, with S representing 4 layers of voxel hierarchies and M varying across different datasets. The total training loss, \mathcal{L}_{total} , is a weighted sum of losses for structural prediction, voxel-level normal supervision, and surface geometry. The structure loss, \mathcal{L}_{struct} , is a multi-level cross-entropy loss that supervises voxel occupancy at different depths d of the hash tree. The voxel normal loss, $\mathcal{L}_{\text{vox normal}}$, uses an L1 distance to enforce consistency between predicted and ground-truth normals on the grid. The surface geometry loss combines a surface loss \mathcal{L}_f , which forces the implicit function f to be zero on the surface, and a gradient loss $\mathcal{L}_{\text{grad}}$, which aligns the predicted gradient ∇f with the ground-truth surface normal \mathbf{n}_{gt} using a dot product. The complete loss function can be summarized by the following equation:

$$\mathcal{L}_{\text{total}} = \sum_{d} w_{\text{struct}} \cdot \mathcal{L}_{\text{struct},d} + \sum_{d} w_{\text{vox}} \cdot \mathcal{L}_{\text{vox_normal},d} + \mathbb{I}_{\text{full}} \cdot w_{\text{surf}} \left(\mathcal{L}_f + w_{\text{grad}} \mathcal{L}_{\text{grad}} \right),$$
(17)

Where d is the depth on voxel hierarchy S. \mathbb{I}_{full} is an indicator function that is 0 during the fist training phase and 1 otherwise. w_{struct} , w_{vox} , w_{surf} , and w_{grad} are the respective weights for each loss component from the hyperparameters. The efficacy of these parameter selections will be explored further in our forthcoming ablation studies. Supervision is provided using 10000 points on Matterport3D and 1000/3000 points on ShapeNet dataset. We train our model on an NVIDIA V100 GPU with 32GB memory and an Intel Xeon E5-2698 v4 CPU.

B. Evaluation Metrics

We evaluate the reconstruction quality using several standard metrics: F-Score (%) (\uparrow), which balances precision and recall; Chamfer Distance (\downarrow), the L1 distance between prediction and ground truth; Normal Consistency (%) (\uparrow), the alignment of surface normals; and Intersection-over-Union (IoU) (\uparrow), the volumetric accuracy for watertight meshes.

C. Object-level Reconstruction

In the context of object-level evaluations, we utilize the ShapeNet datasets [51], which comprises a comprehensive collection of over 50,000 unique three-dimensional models specifically curated for deep learning applications. Consistent with established protocols in the field, we employ the trainvalidation-test partition proposed by [4], which encompasses thirteen distinct object categories. A total of 8,751 previously unseen objects across these categories are employed for benchmarking purposes. Following the methodology of [5], we generate virtually-fused watertight meshes to serve as ground truth, as opposed to utilizing the original raw meshes that may not adhere to manifold constraints. All meshes are normalized to fit within a unit cube. Our experimental framework is structured around three distinct scenarios: 'No noise, 1K points', 'Small noise, 3K points', and 'Large noise, 3K points'. Here, 'small noise' and 'large noise' pertain to Gaussian noise perturbations superimposed on the input point sets, with standard deviations of 0.005 and 0.025, respectively.

Given the approximately uniform geometric variations observed in the ShapeNet objects, with few instances of less detailed surfaces such as planes, we deem the implementation of an adaptive voxel grid structure unnecessary for this dataset. Consequently, we set the maximum adaptive depth, M, to 1, signifying that voxels at scales s>1 are not preserved in their original form. In constructing the ground-truth voxel grid for structural supervision $(c_k^s)_g t$, we ensure that each point on the ground-truth surface is encapsulated by a voxel at all scales.

TABLE I
SHAPENET OBJECT-LEVEL RECONSTRUCTION RESULTS

Method	No noise, 1K points				Small noise, 3K points			Large noise, 3K points				
	Chamfer ↓	F-score ↑	Normal C. ↑	IoU ↑	Chamfer ↓	F-score ↑	Normal C. ↑	IoU ↑	Chamfer ↓	F-score ↑	Normal C. ↑	IoU ↑
ConvONet	6.38	88.2	92.0	81.6	4.65	93.4	93.5	87.4	7.69	80.9	90.7	77.8
NGSolver	3.07	97.1	94.4	91.3	3.03	98.4	94.7	91.3	5.24	89.4	91.6	82.1
NKSR	2.54	97.6	94.3	92.7	2.57	98.7	94.6	91.8	5.01	89.8	91.4	82.1
Ours	2.71	98.5	95.9	94.0	2.77	99.1	96.0	93.0	5.03	90.4	92.1	82.7

A voxel size of b = 0.02 has been determined sufficient for accurately modeling the shapes in question.

In our study, we compare our approach against several established baselines including the Screened Poisson Surface Reconstruction (SPSR) as detailed in [11], Convolutional Occupancy Networks (ConvONet) reported by [17], Neural Galerkin(NGSolver) by [27], and NKSR from [16]. All learnable models were retrained from the ground up.

The results of these comparisons are summarized in Table I and visually presented in Figure 3. The non-learnable modules SPSR struggle to reconstruct detailed geometries from sparse datasets as small as 1K points and are notably affected by noise, which leads to distorted, bulging geometrical outputs. Additionally, our method demonstrates superior reconstruction accuracy over ConvONet. This is notable since ConvONet infers implicit fields directly without any guarantees of fit.

Our method's voxel grid resolution is comparable to that of ConvONet, which uses neural-network-parameterized local implicit fields. However, our approach achieves approximately a 9% higher F-score, underscoring the robust representational capabilities of our elementary-function-based bases. Unlike NGSolver, which tackles a screened variant of the Poisson equation using a discrete grid, our method employs a Hessian-based regularizer to enforce smoothness, thereby capturing more detailed and faithful models of the shapes with a highly accurate SDF gradient field.

D. Room-level Reconstruction

The scalability of our approach is further validated on the Matterport3D dataset [52], which comprises real-world scans of indoor environments captured using a panoramic depth camera. This dataset includes a total of 90 buildings. Adhering to the prescribed train/test division, we further segment each building into discrete rooms, each of which is reconstructed and assessed independently. The test dataset encompasses 399 rooms. For supervisory data generation, we employ the methodology outlined in § 5.3, which generates larger-scale voxels in planar areas such as walls and floors. We configure our system with M=2 and b=0.012.

While the indoor scans consist solely of single-sided surfaces, our solver's tendency to produce watertight geometries results in the presence of minimal floaters at the domain boundaries. Utilizing a truncated domain Ω , these floaters are contained within a small area and are strategically prevented from emerging in areas distant from the surface. In our evaluations, we implement a k-nearest neighbors (k-NN) strategy to eliminate vertices on the produced mesh that are excessively distant from the input points. For quantitative evaluations, we adhere to established protocols and reduce the

TABLE II
MATTERPORT3D ROOM-LEVEL RECONSTRUCTION RESULTS

Method	No noise, 10K points			
	Chamfer ↓	F-score ↑	Normal C. ↑	
ConvONet	6.21	88.9	92.3	
NGSolver	3.79	93.5	94.3	
NKSR	2.60	96.4	96.5	
Ours	3.07	97.9	94.9	

input point cloud to 10K points. We benchmarked our method against ConvONet, NGSolver and NKSR. The outcomes of the comparative analysis are meticulously presented in Table II and visually represented in Figure 4. Our approach consistently surpasses all comparative benchmarks in F-score, the primary metric for reconstruction accuracy, delivering precise and detailed reconstructions at the room level with intricate geometric nuances. Notably, our methodology demonstrates a natural benefit wherein the accuracy of reconstruction progressively improves as more input data points are provided, without requiring modifications to the network architecture—a characteristic not regularly observed in several contemporary learning-based models, such as ConvONet.

E. Evaluation on Surface Reconstruction Benchmark

We further evaluate our method on the Surface Reconstruction Benchmark (SRB), comparing it against leading baselines. Following the standard protocol, all methods process an input of 3,000 points, and learning-based models are trained on ShapeNet. Table III summarizes the quantitative results. Our approach demonstrates superior performance, which underscores its strong generalization capabilities.

For qualitative assessment, as illustrated in Figure 5, we compare our method with state-of-the-art approaches like NKSR and NGSolver. NKSR tends to produce overly smooth surfaces, sacrificing fine geometric details. In contrast, NG-Solver preserves details to an extent that results in a rough and noisy surface. Our method strikes a better balance, effectively capturing the overall object semantics while retaining crucial details.

F. Ablation Studies

Ablation experiments are executed utilizing the ShapeNet and Matterport datasets. Specifically, for ShapeNet, the 'Small noise, 3K points' configuration is selected, focusing on its chair category for all phases: training, validation, and testing. Under identical parameter settings, our model, trained solely on this subset, demonstrates comparable performance to that

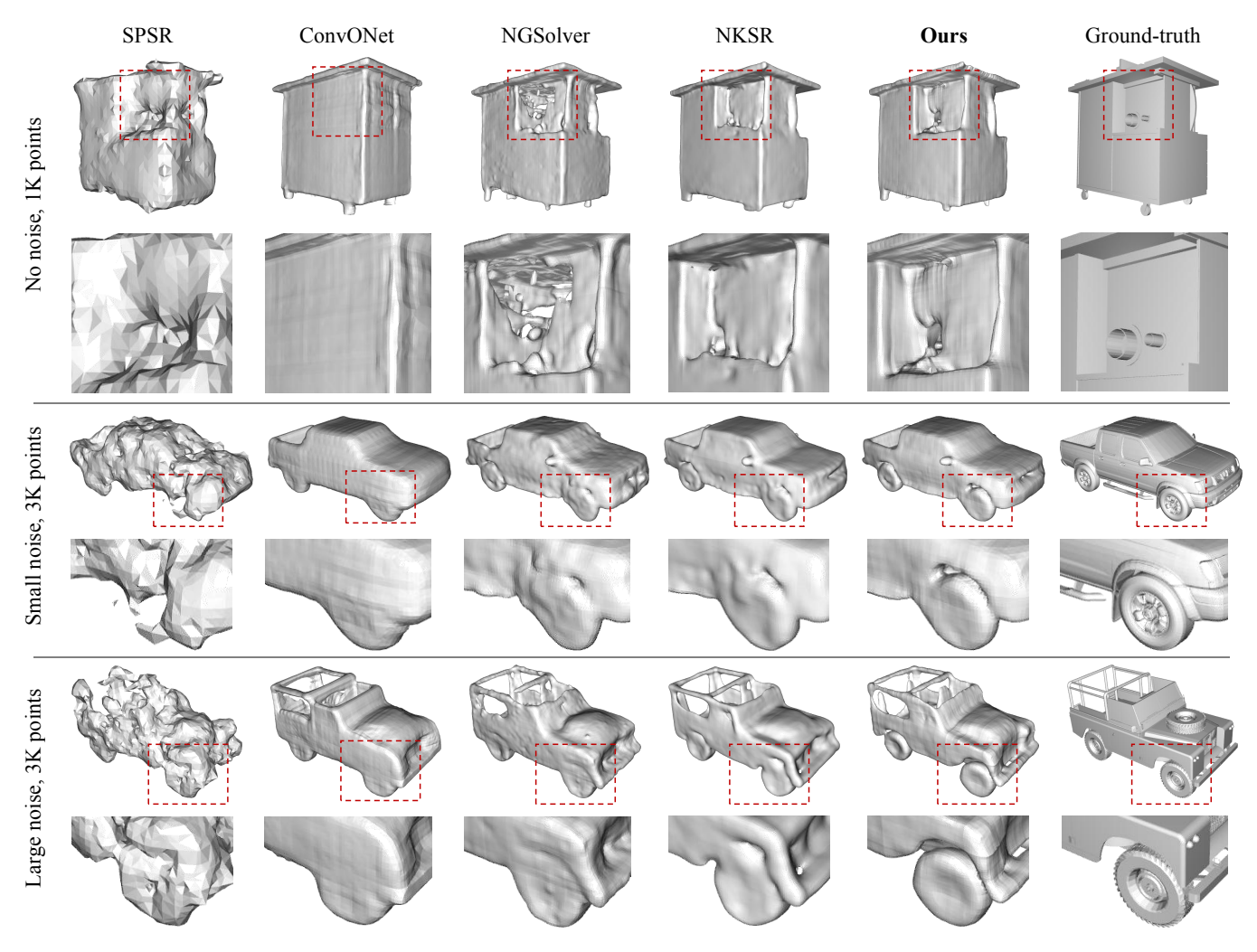


Fig. 3. Here are the results on the ShapeNet dataset [51] across three different settings. Methods SPSR utilize points normals, while others do not. Notably, our method demonstrates a capability to accurately reconstruct fine geometric details (such as the car wheels).

TABLE III

QUANTITATIVE COMPARISON ON THE SURFACE RECONSTRUCTION
BENCHMARK (SRB). BEST RESULTS ARE IN BOLD.

Method	Chamfer $\times 10^{-2} \downarrow$	F-Score (%) ↑	Normal C. ↑
OG-INR [24]	8.988	11.1	59.1
ImplicitFilter [48]	3.764	31.9	79.6
POCO [19]	1.255	73.4	92.0
ALTO [34]	1.245	71.8	90.3
NKSR [16]	1.118	76.1	93.2
NGSolver [27]	1.105	76.9	93.0
Ours	1.099	77.2	93.4

trained on the comprehensive dataset (F-score 98.4 versus 98.6). Beyond the F-score and normal consistency metrics, we transition the chamfer distance metric from the L1-norm to the L2-norm (hereinafter referred to as 'L2-Chamfer') to enhance the visibility of differences, given its sensitivity to outliers. The L2 distance is adjusted by a factor of 10^5 to facilitate clearer visualization.

1) Energy formulation with Hessian regularization: The balancing factor λ_2 , as defined in Equation 6, is employed to

TABLE IV Performance Metrics for Various λ_2 Settings.

λ_2	Chamfer $\times 10^{-3}$ ↓	F-score ↑	Normal C. ↑
0.0	3.00	98.2	93.7
2.0	2.92	98.4	93.8
3.0	2.55	98.5	93.9
6.0	2.91	98.4	98.9

ensure the smoothness of the SDF gradient field by constraining the norm of the Hessian matrix. In scenarios where λ_2 equals zero, the approach reverts to a basic Screened Poisson solution, as described by [11], with a sole focus on the normal data, which in our implementation is predicted by the network. As depicted in TABLE IV, all metrics show improvement with $\lambda=3$. These findings demonstrate the significant role of the Hessian regularization term in producing higher-quality geometrical constructs. It is essential to recognize that the elements in Equation 6, aside from λ_2 , are pivotal, offering critical guidance for determining the surface location and orientation. Notably, the absence of these terms in Equation (5), specifically as λ approaches infinity, results in the non-

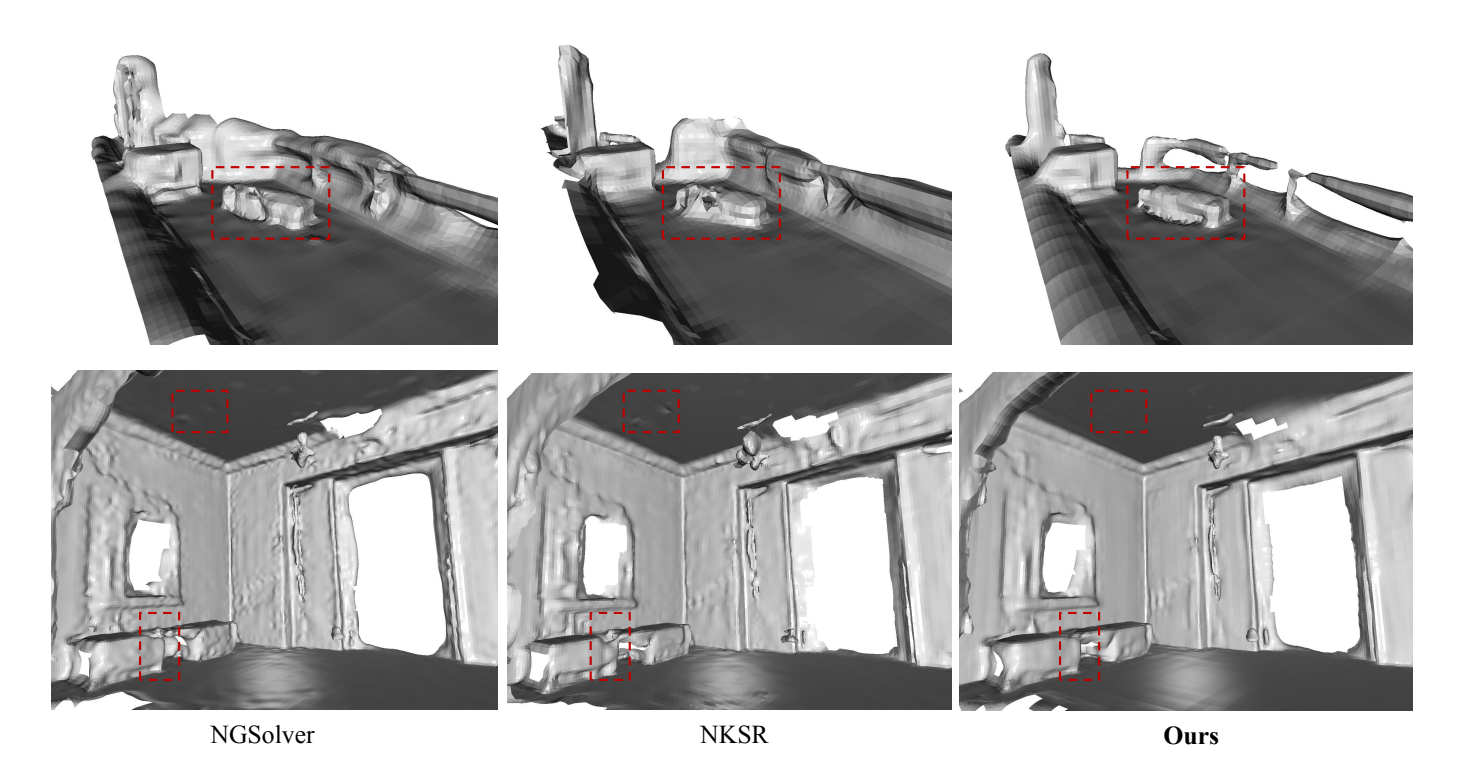


Fig. 4. Qualitative results on the Matterport3D dataset. Our method demonstrates superior performance in reconstructing large-scale indoor scenes, excelling at capturing fine details, such as the chair highlighted in the red box, while simultaneously ensuring overall structural integrity by eliminating noise from surfaces like walls and floors.

convergence of our solver.

2) Multi-Layer Convolution: We conducted an ablation study to ascertain the efficacy of multi-layer convolution in the context of adaptive sparse neural networks applied to sparse voxel hierarchies for surface reconstruction tasks. The study comprised three distinct experimental setups: (1) a baseline model without multi-layer convolution, (2) a model integrating multi-layer convolution within the encoder, and (3) a model employing multi-layer convolution across both the encoder and decoder. The inclusion of multi-layer convolutions is intended to facilitate a more nuanced aggregation of point information across varying densities of input point clouds, thereby enhancing the model's ability to capture and utilize complex spatial hierarchies.

The performance of each configuration was rigorously evaluated against three critical metrics: Chamfer Distance, F-Score, and Normal Consistency, as shown in the table below. The results distinctly illustrate the substantial gains in performance metrics when multi-layer convolutions are implemented, particularly when incorporated throughout both the encoder and decoder. This configuration yielded the highest scores across all evaluated metrics, substantiating the proposed hypothesis regarding the advantages of multi-layer convolution in handling complex and non-uniform datasets.

3) Point-Voxel Attention: To validate the effectiveness of the Point-Voxel Attention mechanism, we conducted an ablation study by comparing the model's performance with and without this component. The results, summarized in Table VI, demonstrate a clear improvement across all key metrics when the Point-Voxel Attention is integrated.

TABLE V
PERFORMANCE COMPARISON OF DIFFERENT CONFIGURATIONS.
MLC: MULTI-LAYER CONVOLUTION, ENC.: ENCODER, DEC.: DECODER

Config.	Chamfer $\times 10^{-3} \downarrow$	F-score ↑	Normal C. ↑
No MLC	3.03	98.12	93.4
Enc. + MLC	2.95	98.29	93.7
Enc. & Dec. + MLC	2.92	98.34	93.8

 $\begin{tabular}{ll} TABLE\ VI \\ ABLATION\ STUDY\ OF\ THE\ POINT-VOXEL\ ATTENTION\ (PVA)\ MECHANISM. \end{tabular}$

Method	Chamfer $\times 10^{-3} \downarrow$	F-score ↑	Normal C. ↑
Ours (w/o PVA)	3.17	98.2	94.5
Ours (w/ PVA)	3.01	98.6	94.9

Specifically, the inclusion of Point-Voxel Attention leads to a lower Chamfer Distance, a higher F-score, and improved Normal Consistency . This indicates that our attention mechanism effectively enhances the model's ability to capture fine-grained geometric details and produce more accurate surface reconstructions. The performance gains underscore the importance of aggregating features from both point and voxel representations for high-fidelity shape completion.

G. Computational Efficiency Analysis

To evaluate the practical applicability of our method, we conducted a comprehensive analysis of computational time and memory usage across different configurations. All experiments were performed on a workstation equipped with an NVIDIA RTX 4090 GPU and 64GB RAM.

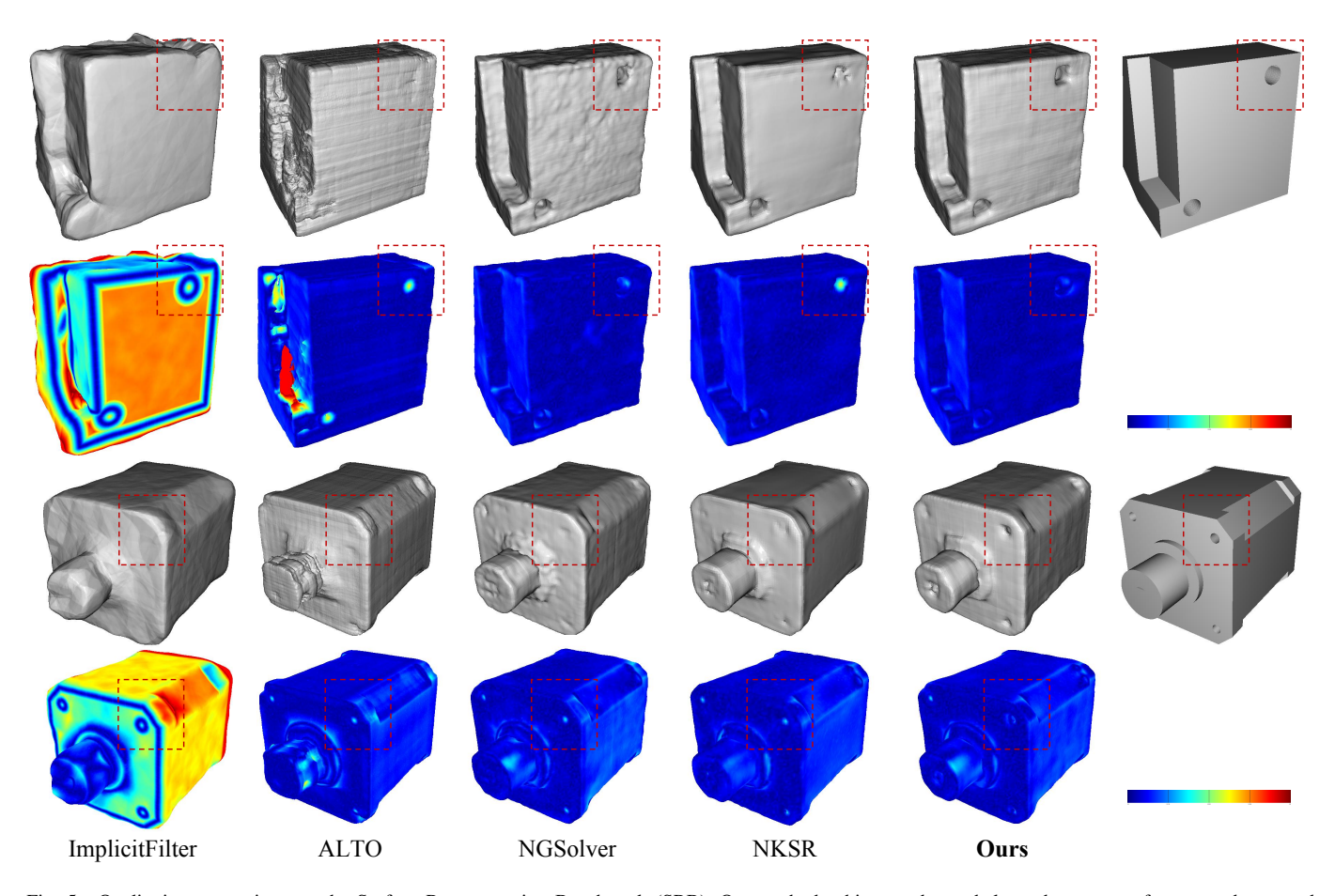


Fig. 5. Qualitative comparison on the Surface Reconstruction Benchmark (SRB). Our method achieves a better balance between surface smoothness and detail preservation. The error is visualized with a color map where blue indicates low error and red indicates high error.

TABLE VII

COMPUTATIONAL EFFICIENCY COMPARISON ACROSS DIFFERENT METHODS.

Method	Inference Time (s)	Memory Usage (GB)
ImplicitFilter [48]	30.3	2.1
OG-INR [24]	18.5	5.54
POCO [19]	5.3	4.6
ALTO [34]	4.5	3.8
Ours	2.5	4.1

The efficiency analysis reveals that our method achieves competitive computational performance while maintaining superior reconstruction quality. Although the full configuration requires slightly more computational resources than the baseline, the increase is marginal compared to the significant quality improvements observed. Notably, our method demonstrates faster inference times compared to traditional methods like ImplicitFilter and OG-INR, while achieving substantially better reconstruction quality with a comparable memory footprint.

V. CONCLUSION

In this research paper, we introduce NeuralSSD, an innovative framework for 3D surface reconstruction that generates an implicit 3D surface from commonly available point cloud data. Through comprehensive experiments, we demonstrate

that our method achieves a desirable balance between point fitting fidelity and strong generalization capabilities to different objects. We believe that our approach enables higher-definition outputs, demonstrates good generalization to unseen data, and makes deep-learning-based surface reconstruction more accessible for various applications. As part of future research, we aim to enhance the reconstruction quality by exploring alternative families of basis functions. Additionally, we plan to reduce the memory footprint to enable larger-scale reconstructions.

VI. BIOGRAPHY SECTION



Zi-Chen Xi is a Master's candidate at the Departemnt of Computer Science and Technology, Tsinghua University. He previously received his Bachelor's degree in Architecture from the School of Architecture at Tsinghua University in 2022. His research interests lie in 3D computer vision and computer graphics.



Tai-Jiang Mu is currently an assistant researcher at Tsinghua University, where he received his B.S. and Ph.D. degrees in Computer Science in 2011 and 2016, respectively. His research interests include computer graphics, computer vision and image processing. He has published more than 40 papers in refereed journals and conferences, including IEEE TPAMI, ACM TOG, IEEE TVCG, IEEE TIP, CVMJ, CVPR, AAAI, ECCV, ICRA, etc. He is the on the editorial board of the Visual Computer.



Jiahui Huang is currently a research scientist at NVIDIA Toronto AI Lab led by Sanja Fidler. He received my Ph.D. in 2023 from the Graphics and Geometric Computing Group at Tsinghua University, China, advised by Shi-Min Hu. He was also a visiting researcher in the Geometric Computing group at Stanford University, led by Leonidas Guibas. His primary research interest lies in the joint lield of 3D computer vision and graphics, including neural reconstruction, dynamic scene perception, and SLAM.



Shi-Min Hu is currently a professor in Computer Science at Tsinghua University. He received a Ph.D. degree from Zhejiang University in 1996. His research interests include geometry processing, image & video processing, rendering, computer animation, and CAD. He has published more than 100 papers in top tier journals and conferences. He is the Editorin-Chief of Computational Visual Media, and on the editorial boards of several journals, including Computer Aided Design and Computer & Graphics.



Hao-Xiang Chen received his bachelor's degree in computer science from JiLin University in 2020. He is currently a PhD candidate in the Department of Computer Science and Technology, Tsinghua University. His research interests include 3D reconstruction and 3D computer vision.



Francis Williams is a senior research scientist at NVIDIA in NYC working at the intersection of computer vision, machine learning, and computer graphics. His research is a mix of theory and application, aiming to solve practical problems in elegant ways. In particular, he is very interested in 3D shape representations which can enable deep learning on "real-world" geometric datasets which are often noisy, unlabeled, and consisting of very large inputs. He completed my PhD from NYU in 2021 where he worked in the Math and Data Group

and the Geometric Computing Lab. His advisors were Joan Bruna and Denis Zorin.



Qun-Ce Xu is a postdoctoral researcher in the Department of Computer Science and Technology at Tsinghua University, Beijing, China. He received his Ph.D. degree from the University of Bath, UK, in 2021. His research interests include geometric learning, geometry processing and shape generation.

REFERENCES

- F. Calakli and G. Taubin, "Ssd: Smooth signed distance surface reconstruction," in <u>Computer Graphics Forum</u>, vol. 30, no. 7. Wiley Online Library, 2011, pp. 1993–2002.
- [2] J. C. Carr, R. K. Beatson, J. B. Cherrie, T. J. Mitchell, W. R. Fright, B. C. McCallum, and T. R. Evans, "Reconstruction and representation of 3d objects with radial basis functions," in <u>Proceedings of the 28th annual conference on Computer graphics and interactive techniques</u>, 2001, pp. 67–76.
- [3] F. Williams, T. Schneider, C. Silva, D. Zorin, J. Bruna, and D. Panozzo, "Deep geometric prior for surface reconstruction," in <u>Proceedings of the IEEE/CVF conference on computer vision and pattern recognition</u>, 2019, pp. 10130–10139.
- [4] C. B. Choy, D. Xu, J. Gwak, K. Chen, and S. Savarese, "3d-r2n2: A unified approach for single and multi-view 3d object reconstruction," in Computer Vision–ECCV 2016: 14th European Conference, Amsterdam, The Netherlands, October 11-14, 2016, Proceedings, Part VIII 14. Springer, 2016, pp. 628–644.
- [5] L. Mescheder, M. Oechsle, M. Niemeyer, S. Nowozin, and A. Geiger, "Occupancy networks: Learning 3d reconstruction in function space," in Proceedings of the IEEE/CVF conference on computer vision and pattern recognition, 2019, pp. 4460–4470.
- [6] M. Tatarchenko, S. R. Richter, R. Ranftl, Z. Li, V. Koltun, and T. Brox, "What do single-view 3d reconstruction networks learn?" in <u>Proceedings</u> of the IEEE/CVF conference on computer vision and pattern recognition, 2019, pp. 3405–3414.
- [7] W. E. Lorensen and H. E. Cline, "Marching cubes: A high resolution 3d surface construction algorithm," in <u>Seminal graphics: pioneering efforts</u> that shaped the field, 1998, pp. 347–353.
- [8] B. Curless and M. Levoy, "A volumetric method for building complex models from range images," in Proceedings of the 23rd annual conference on Computer graphics and interactive techniques, 1996, pp. 303–312.
- [9] Y. Ohtake, A. Belyaev, M. Alexa, G. Turk, and H.-P. Seidel, "Multi-level partition of unity implicits," in <u>Acm Siggraph 2005 Courses</u>, 2005, pp. 173–es.
- [10] M. Kazhdan, M. Bolitho, and H. Hoppe, "Poisson surface reconstruction," in Proceedings of the fourth Eurographics symposium on Geometry processing, vol. 7, no. 4, 2006.
- [11] M. Kazhdan and H. Hoppe, "Screened poisson surface reconstruction," ACM Transactions on Graphics (ToG), vol. 32, no. 3, pp. 1–13, 2013.
- [12] I. Vizzo, X. Chen, N. Chebrolu, J. Behley, and C. Stachniss, "Poisson surface reconstruction for lidar odometry and mapping," in 2021 IEEE international conference on robotics and automation (ICRA). IEEE, 2021, pp. 5624–5630.
- [13] L. Chu, H. Pan, and W. Wang, "Unsupervised shape completion via deep prior in the neural tangent kernel perspective," <u>ACM Transactions on Graphics (TOG)</u>, vol. 40, no. 3, pp. 1–17, 2021.
- [14] F. Williams, Z. Gojcic, S. Khamis, D. Zorin, J. Bruna, S. Fidler, and O. Litany, "Neural fields as learnable kernels for 3d reconstruction," in Proceedings of the IEEE/CVF Conference on Computer Vision and Pattern Recognition, 2022, pp. 18500–18510.
- [15] F. Williams, M. Trager, J. Bruna, and D. Zorin, "Neural splines: Fitting 3d surfaces with infinitely-wide neural networks," in <u>Proceedings of the</u> <u>IEEE/CVF Conference on Computer Vision and Pattern Recognition</u>, 2021, pp. 9949–9958.
- [16] J. Huang, Z. Gojcic, M. Atzmon, O. Litany, S. Fidler, and F. Williams, "Neural kernel surface reconstruction," in <u>Proceedings of the IEEE/CVF Conference on Computer Vision and Pattern Recognition</u>, 2023, pp. 4369–4379.
- [17] S. Peng, M. Niemeyer, L. Mescheder, M. Pollefeys, and A. Geiger, "Convolutional occupancy networks," in Computer Vision–ECCV 2020: 16th European Conference, Glasgow, UK, August 23–28, 2020, Proceedings, Part III 16. Springer, 2020, pp. 523–540.
- [18] H.-X. Chen, J. Huang, T.-J. Mu, and S.-M. Hu, "Circle: Convolutional implicit reconstruction and completion for large-scale indoor scene," in <u>European Conference on Computer Vision</u>. Springer, 2022, pp. 506– 522.
- [19] A. Boulch and R. Marlet, "Poco: Point convolution for surface reconstruction," in Proceedings of the IEEE/CVF Conference on Computer Vision and Pattern Recognition, 2022, pp. 6302–6314.
- [20] B. Ummenhofer and V. Koltun, "Adaptive surface reconstruction with multiscale convolutional kernels," in <u>Proceedings of the IEEE/CVF</u> International Conference on Computer Vision, 2021, pp. 5651–5660.

- [21] P.-S. Wang, Y. Liu, and X. Tong, "Dual octree graph networks for learning adaptive volumetric shape representations," <u>ACM Transactions</u> on Graphics (TOG), vol. 41, no. 4, pp. 1–15, 2022.
- [22] Z. Wang, P. Wang, P. Wang, Q. Dong, J. Gao, S. Chen, S. Xin, C. Tu, and W. Wang, "Neural-imls: Self-supervised implicit moving least-squares network for surface reconstruction," <u>IEEE Transactions on Visualization</u> and Computer Graphics, 2023.
- [23] Y. Ben-Shabat, C. H. Koneputugodage, and S. Gould, "Digs: Divergence guided shape implicit neural representation for unoriented point clouds," in Proceedings of the IEEE/CVF conference on computer vision and pattern recognition, 2022, pp. 19323–19332.
- [24] C. H. Koneputugodage, Y. Ben-Shabat, and S. Gould, "Octree guided unoriented surface reconstruction," in <u>Proceedings of the IEEE/CVF</u> <u>Conference on Computer Vision and Pattern Recognition</u>, 2023, pp. 16717–16726.
- [25] G. Yuan, Q. Fu, Z. Mi, Y. Luo, and W. Tao, "Ssrnet: Scalable 3d surface reconstruction network," <u>IEEE Transactions on Visualization and Computer Graphics</u>, vol. 29, no. 12, pp. 4906–4919, 2023.
- [26] S. Peng, C. Jiang, Y. Liao, M. Niemeyer, M. Pollefeys, and A. Geiger, "Shape as points: A differentiable poisson solver," <u>Advances in Neural Information Processing Systems</u>, vol. 34, pp. 13 032–13 044, 2021.
- [27] J. Huang, H.-X. Chen, and S.-M. Hu, "A neural galerkin solver for accurate surface reconstruction," <u>ACM Transactions on Graphics (TOG)</u>, vol. 41, no. 6, pp. 1–16, 2022.
- [28] R. Hanocka, G. Metzer, R. Giryes, and D. Cohen-Or, "Point2mesh: a self-prior for deformable meshes," <u>ACM Transactions on Graphics</u> (TOG), vol. 39, no. 4, pp. 126–1, 2020.
- [29] J. J. Park, P. Florence, J. Straub, R. Newcombe, and S. Lovegrove, "Deepsdf: Learning continuous signed distance functions for shape representation," in Proceedings of the IEEE/CVF conference on computer vision and pattern recognition, 2019, pp. 165–174.
- [30] M. Atzmon and Y. Lipman, "Sald: Sign agnostic learning with derivatives," in International Conference on Learning Representations.
- [31] Y. Lipman, "Phase transitions, distance functions, and implicit neural representations," in <u>Proceedings of the 38th International Conference</u> on Machine Learning, 2021, pp. 6702–6712.
- [32] B. Ma, Z. Han, Y.-S. Liu, and M. Zwicker, "Neural-pull: Learning signed distance function from point clouds by learning to pull space onto surface," in International Conference on Machine Learning. PMLR, 2021, pp. 7246–7257.
- [33] B. Ma, Y.-S. Liu, and Z. Han, "Learning signed distance functions from noisy 3d point clouds via noise to noise mapping," 2023.
- [34] Z. Wang, S. Zhou, J. J. Park, D. Paschalidou, S. You, G. Wetzstein, L. Guibas, and A. Kadambi, "Alto: Alternating latent topologies for implicit 3d reconstruction," in Proceedings of the IEEE/CVF Conference on Computer Vision and Pattern Recognition, 2023, pp. 259–270.
- [35] T. Müller, A. Evans, C. Schied, and A. Keller, "Instant neural graphics primitives with a multiresolution hash encoding," <u>ACM transactions on</u> graphics (TOG), vol. 41, no. 4, pp. 1–15, 2022.
- [36] G. Riegler, A. Osman Ulusoy, and A. Geiger, "Octnet: Learning deep 3d representations at high resolutions," in <u>Proceedings of the IEEE</u> conference on computer vision and pattern recognition, 2017, pp. 3577– 3586
- [37] P.-S. Wang, Y. Liu, Y.-X. Guo, C.-Y. Sun, and X. Tong, "O-cnn: Octree-based convolutional neural networks for 3d shape analysis," <u>ACM Transactions On Graphics (TOG)</u>, vol. 36, no. 4, pp. 1–11, 2017.
- [38] Y. Liao, S. Donne, and A. Geiger, "Deep marching cubes: Learning explicit surface representations," in <u>Proceedings of the IEEE conference</u> on computer vision and pattern recognition, 2018, pp. 2916–2925.
- [39] H. Li, X. Yang, H. Zhai, Y. Liu, H. Bao, and G. Zhang, "Vox-surf: Voxel-based implicit surface representation," <u>IEEE Transactions on Visualization and Computer Graphics</u>, vol. 30, no. 3, pp. 1743–1755, 2022.
- [40] P. Erler, P. Guerrero, S. Ohrhallinger, N. J. Mitra, and M. Wimmer, "Points2surf learning implicit surfaces from point clouds," in <u>European</u> conference on computer vision. Springer, 2020, pp. 108–124.
- [41] R. Chabra, J. E. Lenssen, E. Ilg, T. Schmidt, J. Straub, S. Lovegrove, and R. Newcombe, "Deep local shapes: Learning local sdf priors for detailed 3d reconstruction," in <u>European Conference on Computer Vision</u>. Springer, 2020, pp. 608–625.
- [42] A. Gropp, L. Yariv, N. Haim, M. Atzmon, and Y. Lipman, "Implicit geometric regularization for learning shapes," in <u>Proceedings of the 37th</u> International Conference on Machine Learning, <u>2020</u>, pp. 3789–3799.
- [43] V. Sitzmann, J. Martel, A. Bergman, D. Lindell, and G. Wetzstein, "Implicit neural representations with periodic activation functions," <u>Advances in neural information processing systems</u>, vol. 33, pp. 7462–7473, 2020.

- [44] M. Tancik, P. Srinivasan, B. Mildenhall, S. Fridovich-Keil, N. Raghavan, U. Singhal, R. Ramamoorthi, J. Barron, and R. Ng, "Fourier features let networks learn high frequency functions in low dimensional domains," <u>Advances in neural information processing systems</u>, vol. 33, pp. 7537– 7547, 2020.
- [45] J. N. Martel, D. B. Lindell, C. Z. Lin, E. R. Chan, M. Monteiro, and G. Wetzstein, "Acorn: adaptive coordinate networks for neural scene representation," <u>ACM Transactions on Graphics (TOG)</u>, vol. 40, no. 4, pp. 1–13, 2021.
- [46] T. Takikawa, J. Litalien, K. Yin, K. Kreis, C. Loop, D. Nowrouzezahrai, A. Jacobson, M. McGuire, and S. Fidler, "Neural geometric level of detail: Real-time rendering with implicit 3d shapes," in <u>Proceedings of the IEEE/CVF Conference on Computer Vision and Pattern Recognition</u>, 2021, pp. 11358–11367.
- [47] D. B. Lindell, D. Van Veen, J. J. Park, and G. Wetzstein, "Bacon: Band-limited coordinate networks for multiscale scene representation," in Proceedings of the IEEE/CVF conference on computer vision and pattern recognition, 2022, pp. 16252–16262.
- [48] S. Li, G. Gao, Y. Liu, M. Gu, and Y.-S. Liu, "Implicit filtering for learning neural signed distance functions from 3d point clouds," in <u>European Conference on Computer Vision</u>. Springer, 2024, pp. 234– 251.
- [49] H. Tang, Z. Liu, X. Li, Y. Lin, and S. Han, "Torchsparse: Efficient point cloud inference engine," <u>Proceedings of Machine Learning and Systems</u>, vol. 4, pp. 302–315, 2022.
- [50] S. J. Reddi, S. Kale, and S. Kumar, "On the convergence of adam and beyond," in International Conference on Learning Representations, 2018.
- [51] A. X. Chang, T. Funkhouser, L. Guibas, P. Hanrahan, Q. Huang, Z. Li, S. Savarese, M. Savva, S. Song, H. Su et al., "Shapenet: An informationrich 3d model repository."
- [52] A. Chang, A. Dai, T. Funkhouser, M. Halber, M. Niebner, M. Savva, S. Song, A. Zeng, and Y. Zhang, "Matterport3d: Learning from rgb-d data in indoor environments," in 2017 International Conference on 3D Vision (3DV). IEEE Computer Society, 2017, pp. 667–676.
- [53] J. Zhang, "C-curves: an extension of cubic curves," Computer Aided Geometric Design, vol. 13, no. 3, pp. 199–217, 1996.

APPENDIX

A. Optimal solution to the surface fitting variational problem

Here, we provide a detailed derivation that shows how the energy expression in Equation 6 is transformed into the closed-form solution presented in Equation 9. This transformation is a critical step, as the resulting closed-form expression allows for a direct and efficient computation of the solution.

$$E(f) = \iiint_{\Omega} \left\| \nabla f - \vec{\mathbf{N}} \right\|_{2}^{2} dV$$

$$+ \lambda_{1} \iiint_{\Omega} \left\| H(f) \right\|_{F}^{2} dV$$

$$+ \lambda_{2} \sum_{p \in \mathcal{P}} (f(p) - \xi(p))^{2}$$
(18)

where $1(\cdot)$ denotes the Dirac delta function, which satisfies $\iiint_{\Omega} 1(\mathbf{x}) d\mathbf{x} = 1$ and $1(\mathbf{x}) = 0$ for all $\mathbf{x} \neq 0$.

Since $||H(f)||_F^2$ can be expressed as

$$||H(f)||_F^2 = \sum_i \sum_j \left(\frac{\partial^2 f}{\partial x_i \partial x_j}\right)^2 \tag{19}$$

The Euler-Lagrange equation is a second-order partial differential equation that describes the motion of a system of conservative forces. In the context of surface reconstruction, it is used to find the optimal surface fitting by minimizing the energy of the implicit field f. By extending the Euler-Lagrange equation into a multi-dimensional context, we identify that the stationary points of the energy function E conform to the conditions:

$$\Delta f - \nabla \cdot \vec{\mathbf{N}} + \lambda_1 \sum_{i} \sum_{j} \frac{\partial^2}{\partial x_i \partial x_j} \left(\frac{\partial^2 f}{\partial x_i \partial x_j} \right) + \lambda_2 \sum_{p \in \mathcal{P}} (f(p) - \xi(p)) \mathbb{1}(x - p) = 0 \quad i, j \in \{1, 2, 3\} \quad (20)$$

The third term of Equation 20 can be simplified as follows:

$$\sum_{i} \sum_{j} \frac{\partial^{2}}{\partial x_{i} \partial x_{j}} (\frac{\partial^{2} f}{\partial x_{i} \partial x_{j}}) = \sum_{i} \sum_{j} \frac{\partial^{2}}{\partial x_{i} \partial x_{i}} (\frac{\partial^{2} f}{\partial x_{j} \partial x_{j}}) = \Delta(\Delta f)$$

$$i, j \in \{1, 2, 3\}$$
(21)

This simplification allows us to represent the original Equation 20 in a more concise form:

$$\Delta f - \nabla \cdot \vec{\mathbf{N}} + \lambda_1 \Delta(\Delta f) + \lambda_2 \sum_{p \in \mathcal{P}} (f(p) - \xi(p)) \mathbb{1}(x - p) = 0$$
(22)

Given that a differentiable functional is stationary at its local extrema, the quasi-convex nature of the problem almost certainly yields an optimal solution to the surface fitting energy, which is addressed by our novel geometric solver .

Following the Galerkin method, we transform the strong formulation in Equation (15) into its weak form by introducing a test function ω , leading to:

$$\forall \omega, \iiint_{\Omega} \omega \left(\Delta f - \nabla \cdot \vec{\mathbf{N}} + \lambda_1 \Delta(\Delta f) \right) dx + \lambda_2 \sum_{p \in \mathcal{P}} \omega(p) \left(f(p) - \xi(p) \right) = 0$$
 (23)

The first integral term can be simplified by the integration by parts as $\omega \Delta f = \nabla \cdot (\omega \nabla f) - \nabla f \cdot \nabla \omega$, and by applying Stokes' theorem, which incorporates the boundary conditions over the domain Ω . Subsequently, we replace the arbitrary test functions with the predetermined basis functions, where $f(\mathbf{p}) = \sum_k \bar{\alpha}_k \bar{B}_k(\mathbf{p})$, using the product subscript notation, resulting in the following discretization:

$$\forall \bar{k}, \quad \sum_{\bar{l}} \alpha_{\bar{l}} \iiint_{\Omega} \nabla \mathcal{B}_{\bar{k}}^{\top} \nabla \mathcal{B}_{\bar{l}} dV + \lambda_{2} \sum_{\bar{l}} \alpha_{\bar{l}} \iiint_{\Omega} \Delta \mathcal{B}_{\bar{k}} \cdot \Delta \mathcal{B}_{\bar{l}} dV
+ \lambda_{1} \sum_{\bar{l}} \alpha_{\bar{l}} \sum_{p \in \mathcal{P}} \mathcal{B}_{\bar{k}}(\mathbf{p}) \mathcal{B}_{\bar{l}}(\mathbf{p})
= \iiint_{\Omega} \nabla \mathcal{B}_{\bar{k}}^{\top} \vec{\mathbf{N}} dV + \lambda_{1} \sum_{\mathbf{p} \in \mathcal{P}} \mathcal{B}_{\bar{k}}(\mathbf{p}) \xi(\mathbf{p}) \tag{24}$$

which perfectly aligns with the form $L\alpha = \mathbf{d}$ as specified in Equation 6.

B. Basis functions

The selection of the basis functions B(p), as introduced in Equation 8, is a critical design choice. An appropriate parameterization must be chosen carefully, as it needs to strike a balance between two competing objectives: representational power and computational efficiency. The basis must be diverse enough to represent a wide range of functions, yet simple enough to ensure efficient runtime performance, particularly for the integration required in Equation 9. To address this, we employ a parameterization specifically designed to optimize this trade-off.

We choose the set of elementary functions to be power functions, such as $q_u \in \{1, x, x^2, x^3, \ldots\}$, which make b(x) a polynomial. The piecewise definition of B(p) further leads us to the constraint that b(-1.5) = b(1.5) = 0 and its derivatives $\frac{\partial b}{\partial x}(\pm 1.5) = 0$ for a C^1 -continuous implicit field. To ensure this constraint, we set the coefficients \boldsymbol{m}_k^s to lie within a linear null space defined by these constraints. Although the chosen family of bases consists of simple functions, it still maintains the ability to represent highly complex shapes, similar to the concept of Taylor series. Furthermore, to incorporate high-frequency biases, we introduce sine waves to the set of elementary functions. This Fourier-style family is widely adopted in traditional geometric modeling [53] and modern deep learning [44]. Although this degrades the C^1 -continuity to C^0 , it empirically helps with training.